

Computer vision algorithm for measurement and inspection of O-rings



Gaoliang Peng^{*}, Zhujun Zhang, Wei-quan Li

School of Mechatronics, Harbin Institute of Technology, Harbin 150001, China

ARTICLE INFO

Article history:

Received 4 November 2015

Received in revised form 22 June 2016

Accepted 6 September 2016

Available online 9 September 2016

Keywords:

O-ring

Edge detection

Sub-pixel edge

Least square method

Pattern identification

ABSTRACT

O-rings are one of the most common seals used in industry. Precision measurement and inspection of O-rings play a vital role in seal quality control. Human inspection is a traditional way to remove defective O-rings, which is instable and time consuming. The aim of this paper is to utilize the detection algorithms based on computer vision technology to control the quality of O-rings, which includes the accurate measurement algorithm for the internal/sectional diameter and the classification algorithm for the surface defects. A machine vision system is implemented analyze the captured images of O-rings and perform the measurement and inspection processes. The proposed system is evaluated by inspecting a series of O-rings. Experimental results show that the proposed vision system is capable for measuring and inspecting O-rings seal with good accuracy and efficiency.

© 2016 Elsevier Ltd. All rights reserved.

1. Introduction

Sealing quality is important criteria for the evaluation of equipment quality. Sealing quality will directly affect the accuracy and stability of device. O-ring is currently the most widely used and simple structured sealing element. So ensuring quality of O-rings is particularly important.

Seals are mass-produced, but also require a relatively high quality. Whether the quality of O-rings meets the requirements or not is mainly judged from two aspects. First, the requirement on O-ring size demand that the error of internal dimension and cross-sectional diameter (thickness) must be within the permitted tolerance. Second, the O-ring surface quality requires that O-rings must not have any defects such as material shortage, bumps, dents, and breakage.

The detection of O-rings relies on human inspect currently. Many experienced inspectors detect O-rings in adequate lighting conditions, which is low-accuracy, high in labor-intensity and also time consuming. What's more, it's also instable because the test results are prone to subjective factors. Thus, it is hard to guarantee a stable quality.

Machine vision is an excellent tool for inspecting a variety of items such as textiles, electrical components, and machine tools. With the rapid development of image processing and pattern recognition, machine vision technology have attracted more and

more attentions and is widely used in industry area [1], for its simplicity, noncontact and robustness. However, surface defects inspection is both one of the most common and most difficult problems in the area of machine vision. In literature, many detection technologies have been adopted in industry, such as gear detection [2], bearing inspection [3], and saw detection [4]. Moreover, defects on seal surface often have similar color with their background, which makes it difficult to distinguish the defect from their background. The study of precisely detection for low contrast material is still long way to go. Various techniques used for these aspect have been reviewed by many studies. Martinez et al. [5] designed a machine vision system for surface quality inspection of transparent parts, like headlamp lens. Roby et al. [6] compared four different defect detection algorithms based on Fourier filtering, auto-median, image convolution, and single-step thresholding approaches. Li et al. [7] investigated an appropriate real-time defect detection and location algorithm on surfaces of sequence circular objects. However, the issue of seal surface defect detection has not been previously discussed in these literature yet.

It's very difficult to measure the size accurately and to detect the defect efficiently when contrast of acquired O-rings images is not obvious. Therefore, automatic detection system for O-rings still have much room for improvement. This paper proposes an on-line machine vision system for O-rings quality inspection. A simulation rotating platform and a lighting solution were designed to enhance the contrast of image and make the environment controllable. A series of image processing methods were used to improve the localization accuracy of edge detection. In particular, we compare different defect classification algorithms and select CKFD algorithm to analyze images. The proposed system can achieve size

^{*} Corresponding author.

E-mail addresses: PGL7782@hit.edu.cn (G. Peng), zhangzhujun36@126.com (Z. Zhang), 269338984@qq.com (W. Li).

measurement and defect inspection processes for the O-rings with satisfactory efficiency and accuracy.

The paper is arranged as follows. Section 2 describes the overall layout of the system. In Section 3 we describe edge detection methods for size measurement. The defect detection method is introduced in Section 4. Section 5 includes experiments and discussion. In Section 6 conclusions are drawn.

2. The proposed system

The schematic diagram of the experimental set up used for O seal measurement and inspection is shown in Fig. 1. The hardware consists of a light source, an industrial camera, optical lenses, a computer, an ultra-white glass platform, a light bracket. A simulation platform was set up to simulate the movement of the production line in industrial environment. The ultra-white glass platform, connected to the rotating platform together, can achieve high-precision movement in desired manner under the computer control. The model of rotating platform is HRA200, which has a resolution of 0.01° and a repeat positioning accuracy of 0.005° .

In order to meet requirements of the national testing standard, the measurement accuracy should be higher than 0.08 mm when detecting the O-rings with diameter less than 80 mm. The model of CCD camera is MV-EM510C, which has a resolution of 2456×2058 and the field of view of $100 \text{ mm} \times 100 \text{ mm}$.

The clear surface features and edge profile are needed to measure the size and detect surface defects of O-rings. In this paper, we combine the forward lighting and back lighting [8] as the lighting solution. Two lighting schematics are shown in Fig. 2.

The forward lighting highlighted the surface defects while eliminating the shadow. Back lighting highlighted the edges, and at the same time can eliminate partial reflection of the forward lighting in the ultra-white glass platform. The specific installation form is shown in Fig. 1.

According to the requirement of O-rings inspection, a suitable software was modular designed. The specific process of O-rings quality inspection is shown in Fig. 3. It consists of two separate modules: the size measurement module and defect detection module. Two modules work together to determine whether O-rings are qualified.

As soon as the platform starts to run in a designed manner, software starts to capture images simultaneously. Collected images were analyzed to obtain the current indicators to be detected. It's not necessary to go through the size measurement module if O-rings sample is flawed. So the software was designed to set a flag to indicate the O-rings defect status. When unqualified seals were

detected, the computer marked it out and issued a warning. Otherwise, the system will output the size parameters. All the algorithm detail will be explained in following sections. So the software is capable of processing the size measurement and defect detection simultaneously.

3. The size measurement algorithm

This step measures the inner/outer diameter and the thickness of O-rings. In this process, image noise, positioning accuracy of the edge and the measurement algorithms will have an impact on the accuracy. In the scenario of O-ring seal, we can use the following steps to improve detection accuracy.

3.1. Edge detection with pixel accuracy

Physical contour is one of the most important properties of an object. In order to extract the contour of O-rings, we must detect its edges [9]. The accuracy of edge detection will directly affect the accuracy of dimensional measurements. People have done a lot of research about this, so a lot of methods were developed to detect edges. One can use simple edge detectors like Roberts, Sobel, Prewitt, LoG, or more sophisticated Canny edge detector [10]. All these methods perform edge detection with a pixel accuracy.

For ring detection, we don't need to extract the seal surface texture, since the edge detection is only used to measure the diameter of the inside and outside. And the extracted texture may affect the measurement accuracy. So we can also use the robust morphological edge detectors [11,12], because the morphological methods can eliminate seal surface texture easily. Therefore, an improved anti-noise type morphology edge detection algorithm was used to improve the positioning accuracy by introducing multi-structure elements. In Formula (1), A denotes the original image, S_1 , S_2 , S_3 respectively denote three different structural elements.

$$D_9 = [(A \ominus S_1) \oplus S_2] \oplus S_3 - [(A \oplus S_1) \ominus S_2] \ominus S_3 \quad (1)$$

Fig. 4 shows a comparison of the results by using various algorithms to detect O-rings edge. It can be found that the Roberts, Sobel, Prewitt and LoG edge operator cannot eliminate the unnecessary edges very well. The Canny detector can eliminate some unnecessary edges, but there are still some redundant edges. However, the morphology edge detection algorithm can effectively eliminate the edges of the texture and the reflection-caused edges. So we use morphological edge detection algorithms to extract edges in this machine vision system.

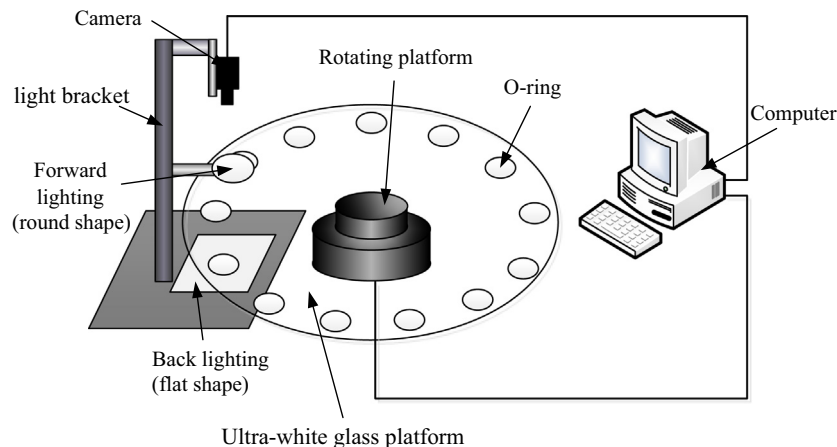


Fig. 1. Schematic of the proposed vision system.

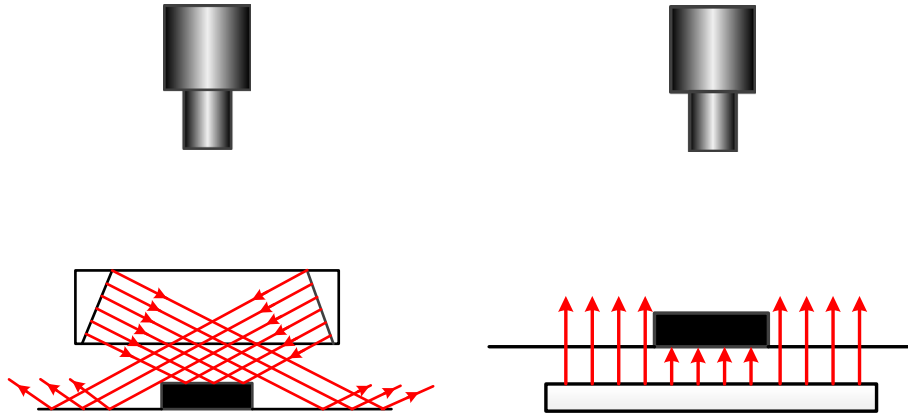


Fig. 2. Schematic of forward lighting and back lighting.

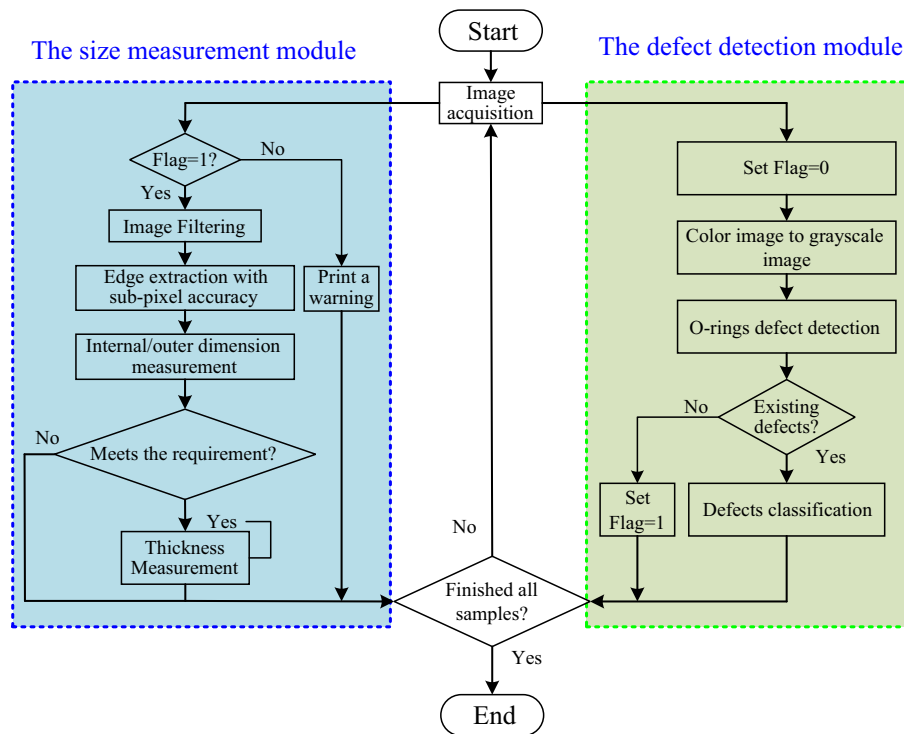


Fig. 3. The specific process of O-rings quality inspection software.

3.2. Edge detection with sub-pixel accuracy

Sometimes it is necessary to detect edges with sub-pixel precision, especially some industrial applications like measurement of the objects with high precision [13]. In order to further improve the measurement accuracy and reduce hardware costs, we have to detect edges with subpixel accuracy. Sub-pixel edge detection is generally determined by pixels around the integer pixel position.

Most sub-pixel edge detectors fall in three groups: fitting, interpolation-based and moment-based methods [14]. After weighing between the requirements on accuracy and computational complexity, a cubic spline interpolation method was selected. This method achieves a sub-pixel accuracy by interpolating the image data to obtain a finer grid of pixels. The ability to obtain accurate interpolation nodes has a direct influence on the accuracy of sub-pixel edge detection. As used herein, the number of nodes is 7.

To determine the interpolation node exactly, we need to know the approximate location of the image edge and the gray gradient direction of it. We should find an edge point of edge detection with pixel accuracy, and mapped a rectangular area of 7×7 around this point, as shown in Fig. 5. Meanwhile, four directions are defined as gray gradient direction in this rectangular area.

a, b, c, d denote four gradient directions, respectively. The angle of adjacent direction is 45° . And the direction is determined by the absolute value sum of difference between the pixel gray scales, which is calculated as:

$$E_i = \sum_{k=0}^6 |p_{k+1} - p_k|, \quad (i = a, b, c, d) \quad (2)$$

The direction of maximum E_i is the gradient direction. And pixels at this direction was extracted as cubic spline interpolation nodes.

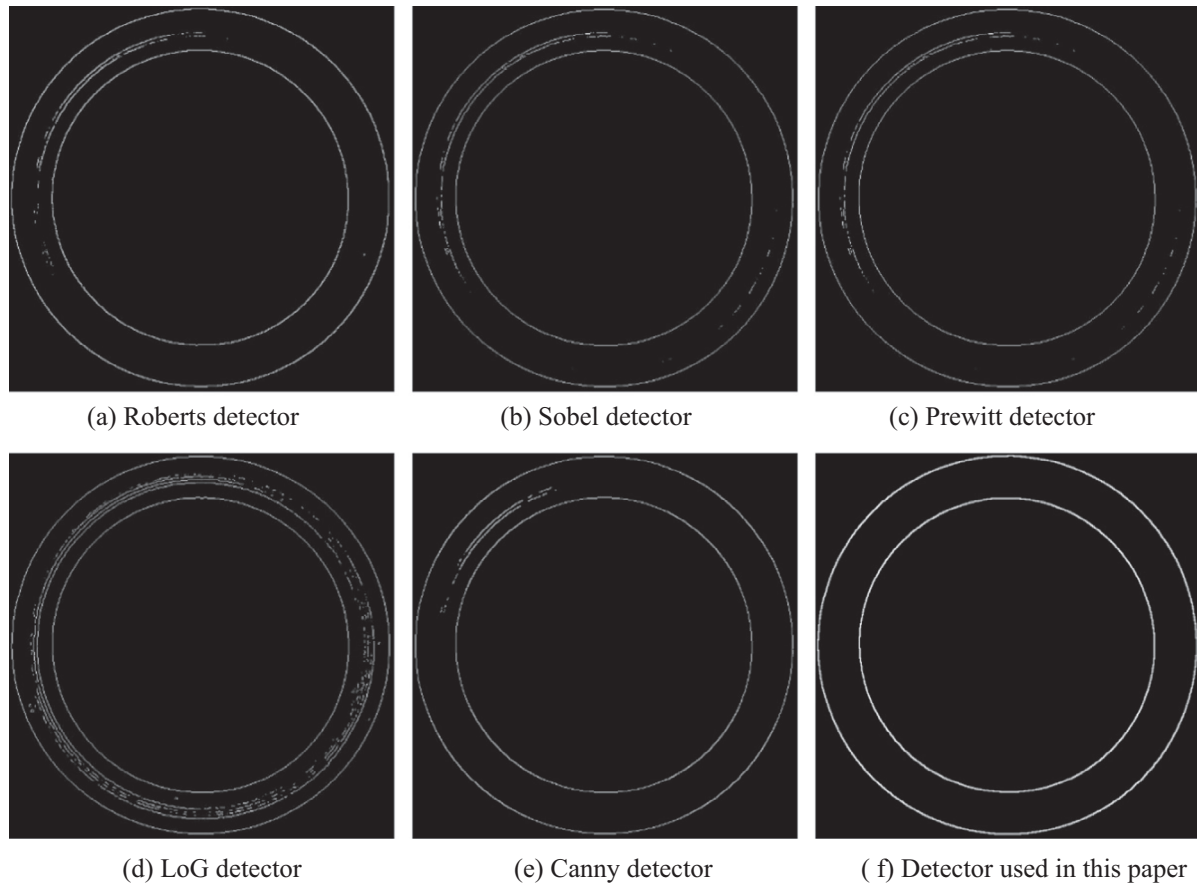


Fig. 4. Performance comparison of various algorithms.

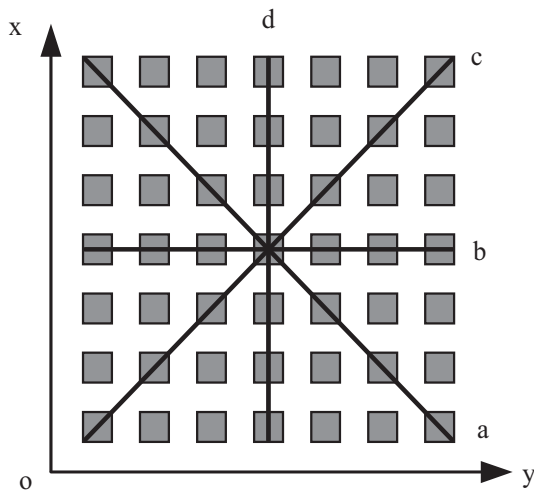


Fig. 5. The schematic of gray gradient directions.

After obtained the integer pixel coordinates and cubic spline function, coordinates of sub-pixels can be calculated through the zero point at second derivative of interpolating function.

So this detection algorithm can be divided into five steps:

- (1) Get the integer pixels, and a rectangular area of 7×7 around it;
- (2) Find the gradient direction, and pick seven points on that direction as interpolation nodes;

- (3) Use nodes from step (2) to set up cubic spline function;
- (4) Calculate the zero point at second derivative of interpolating function to determine sub-pixel points;
- (5) Repeat the previous four steps until all integer pixel edge points are taken.

The flow chart of the above process is shown in Fig. 6.

3.3. Least squares fitting of circles

After sub-pixel edge points are obtained, we need fit them out to measure O-rings diameter and thickness. An improved segmentation algorithm with least squares fitting of circles was used in order to reduce the measurement error [15]. The original image is divided into eight sections. Each section carry out the least squares fitting method according to the sub-pixel position. Then the center coordinates and the radius of each section will be calculated. The perimeter of whole O-ring is the sum of perimeter of each section. Finally, we can get the inner and outer diameters. Thickness of O-ring can be calculated by the subtracting the inner diameter from the outer diameter.

As shown in Fig. 7, the left is one of 8 O-ring sections that need to be extracted, and the right is the corresponding inner edge with integer pixel accuracy. Fig. 8 is the results of extracted sub-pixel edge points.

After applying the least squares fitting method for extracted sub-pixel points in Fig. 8, we can obtain the center coordinates as (351.081, 346.182) and radius as 267.316. The unit is the pixel unit. Fig. 9 shows the arc lines that were fit by least squares fitting method.

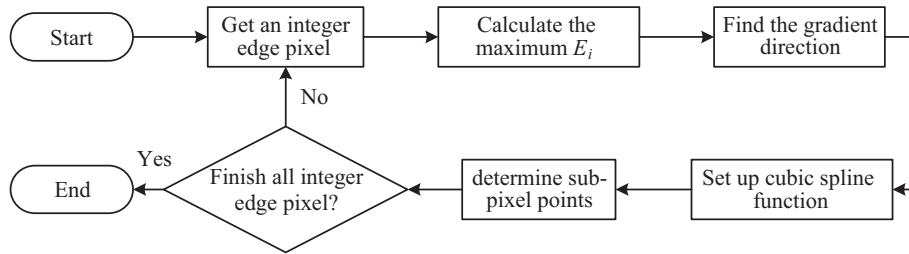


Fig. 6. The flow chart of this algorithm.



Fig. 7. Edge detection of O-rings.

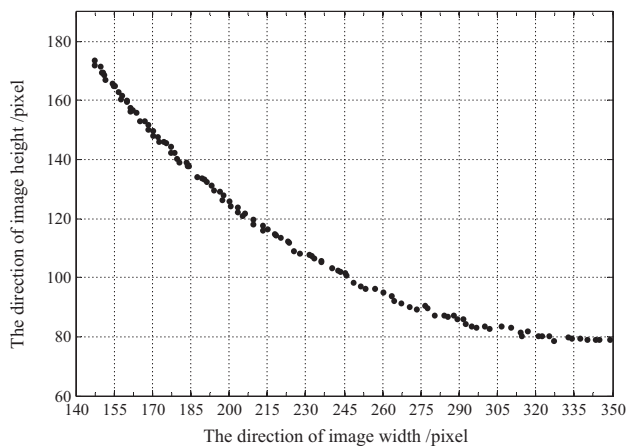


Fig. 8. The corresponding sub-pixel points of Fig. 7.

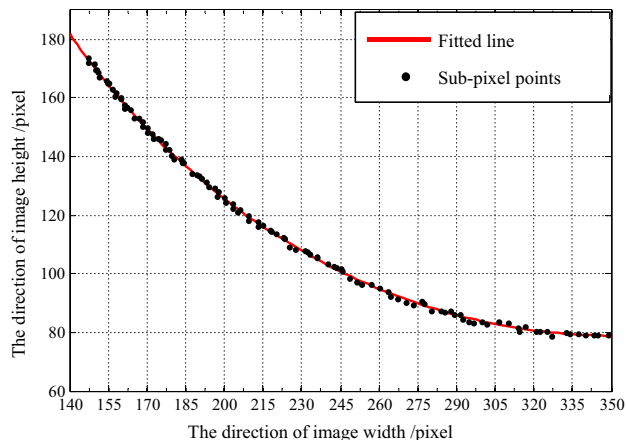


Fig. 9. The arc lines that were fit.

Similarly, we can carry out the fitting for the other 7 sections, and obtain the perimeter of whole O-ring. So the inner diameter was calculated by transferring the pixel units to millimeter with camera pre-calibration. The outer diameter can also be obtained in this way, then thickness is calculated as the difference between the inner and outer diameter.

4. The defect detection algorithm

There are four kinds of typical defect for O-rings, as the material shortage, bumps, dents and breakage. Different features can be extracted to make defect detection and classification. In this section, we evaluate the performance of classification methods with an established database.

4.1. Proposed method

The algorithm for classification should focus on what features are used to represent and how to classify. As the combination of Kernel Principal Components Analysis (KPCA) [16] and Linear Discriminant Analysis (LDA), Complete Kernel Fisher Discriminant Analysis (CKFD) [17] can derive and fuse both regular and irregular information for classification tasks, which make the Kernel Fisher Discriminant Analysis (KFD) [18] more powerful. CKFD can compute the inner products by a kernel function. Polynomial and Gaussian kernel function are widely used in kernel-based classifiers. What's more, the similarity measure have great influence on the performance of classification. So making a comparison between different kernel functions and different similarity measures are essential in our experiments.

The CKFD algorithm is based on a two-phase KFD framework, i.e., LDA and KPCA. Two kinds of discriminant information will be used for classification tasks. The main idea of LDA is to find the subspace that best discriminates different O-rings defect by maximizing the between-class scatter and minimizing the within-class scatter. In LDA, the Fisher criterion functions $J_F(\mathbf{w})$ and $J_b(\mathbf{w})$ can be calculated as follows:

$$J_F(\mathbf{w}) = \frac{\mathbf{w}^T \mathbf{S}_b \mathbf{w}}{\mathbf{w}^T \mathbf{S}_w \mathbf{w}} \quad (3)$$

$$J_b(\mathbf{w}) = \mathbf{w}^T \mathbf{S}_b \mathbf{w} (\|\mathbf{w}\| = 1) \quad (4)$$

where \mathbf{S}_b denotes the between-class scatter matrix and \mathbf{S}_w denotes the within-class scatter matrix.

The CKFD algorithm is to split the KPCA-transformed space R^m into two subspaces, i.e., the null space N and the range space of R . Then the Fisher criterion and the between-class scatter criterion is used to derive the regular discriminant vectors from the range space and irregular discriminant vectors from the null space respectively.

Assumed $\alpha_1, \alpha_2, \dots, \alpha_q, \alpha_{q+1}, \dots, \alpha_m$ as the orthonormal eigenvectors of \mathbf{S}_w . $\Omega_m = \text{span}\{\alpha_1, \alpha_2, \dots, \alpha_q\}$ is the range space R and $\bar{\Omega}_m = \text{span}\{\alpha_{q+1}, \alpha_{q+2}, \dots, \alpha_m\}$ is the null space N . And $R^m = \Omega_m \oplus \bar{\Omega}_m$, where $q = \text{rank}(\mathbf{S}_w)$.

Since Ω_m is isomorphic to space R^q , we can define the corresponding isomorphic mapping as follows:

$$\tilde{\delta} = \mathbf{P}_1 \mathbf{w}, \text{ where } \mathbf{P}_1 = (\alpha_1, \alpha_2, \dots, \alpha_q) \quad (5)$$

Under the mapping, the Fisher criterion function $J_F(\mathbf{w})$ is converted into the equation as follows:

$$J_F(\mathbf{w}) = \frac{\mathbf{w}^T \tilde{\mathbf{S}}_b \mathbf{w}}{\mathbf{w}^T \tilde{\mathbf{S}}_w \mathbf{w}} \quad (6)$$

where $\tilde{\mathbf{S}}_b = \mathbf{P}_1^T \mathbf{S}_b \mathbf{P}_1$ and $\tilde{\mathbf{S}}_w = \mathbf{P}_1^T \mathbf{S}_w \mathbf{P}_1$. The stationary points $\mathbf{v}_1, \mathbf{v}_2, \dots, \mathbf{v}_d$ of $J_F(\mathbf{w})$ are the orthonormal eigenvectors of $\tilde{\mathbf{S}}_b \mathbf{w} = \lambda \tilde{\mathbf{S}}_w \mathbf{w}$ corresponding to the d_{th} largest positive eigenvalues. The optimal regular discriminant vectors $\tilde{\delta}_1, \tilde{\delta}_2, \dots, \tilde{\delta}_d$ can be obtained by $\tilde{\delta}_i = \mathbf{P}_1 \mathbf{v}_i$ ($i = 1, 2, \dots, d$). In a similar way, since $\bar{\Omega}_m$ is isomorphic to Euclidean space R^q ($p = m - q$), we can define the corresponding isomorphic mapping as follows:

$$\hat{\delta} = \mathbf{P}_2 \mathbf{w}, \text{ where } \mathbf{P}_2 = (\alpha_{q+1}, \alpha_{q+2}, \dots, \alpha_m) \quad (7)$$

Under the mapping, the between-class scatter criterion $J_b(\mathbf{w})$ is converted into the equation as follows:

$$J_b(\mathbf{w}) = \mathbf{w}^T \hat{\mathbf{S}}_b \mathbf{w} (\|\mathbf{w}\| = 1) \quad (8)$$

where $\hat{\mathbf{S}}_b = \mathbf{P}_2^T \mathbf{S}_b \mathbf{P}_2$. The stationary points $\mu_1, \mu_2, \dots, \mu_d$ of $J_b(\mathbf{w})$ are the orthonormal eigenvectors of $\hat{\mathbf{S}}_b$ corresponding to the d_{th} largest positive eigenvalues. The optimal irregular discriminant feature vectors $\hat{\delta}_1, \hat{\delta}_2, \dots, \hat{\delta}_d$ can be obtained by $\hat{\delta}_i = \mathbf{P}_2 \mu_i$ ($i = 1, 2, \dots, d$). For a sample vector \mathbf{x} , after being transformed by KPCA, we can acquire a corresponding vector in the transformed space. We can get the regular discriminant feature vector \mathbf{W}_1 and the irregular discriminant vector \mathbf{W}_2 of the vector \mathbf{y} , respectively, as follows:

$$\begin{cases} \mathbf{W}_1 = (\tilde{\delta}_1, \tilde{\delta}_2, \dots, \tilde{\delta}_d)^T \mathbf{y} \\ \mathbf{W}_2 = (\hat{\delta}_1, \hat{\delta}_2, \dots, \hat{\delta}_d)^T \mathbf{y} \end{cases} \quad (9)$$

Finally, we use proper similarity measure to fuse the regular discriminant feature vector \mathbf{W}_1 and the irregular discriminant vector \mathbf{W}_2 .

$$S(W_x, W_y) = k \cdot S(W_{1x}, W_{1y}) + S(W_{2x}, W_{2y}) \quad (10)$$

where $S(W_x, W_y)$ denotes the similarity between the regular discriminant feature and irregular discriminant feature, k denotes the fusion coefficient.

This defect classification algorithm can be divided into five steps:

- (1) Use suitable kernel function to transform the sample into an m dimensional space R^m .
- (2) Construct the between-class and within-class scatter matrices \mathbf{S}_b and \mathbf{S}_w , and then calculate the orthonormal eigenvectors, $\alpha_1, \alpha_2, \dots, \alpha_q, \alpha_{q+1}, \dots, \alpha_m$ of \mathbf{S}_w ;
- (3) Extract the regular discriminant features \mathbf{W}_1 . Let $\mathbf{P}_1 = (\alpha_1, \alpha_2, \dots, \alpha_q)$, calculate the regular discriminant feature vector $\mathbf{W}_1 = (\tilde{\delta}_1, \tilde{\delta}_2, \dots, \tilde{\delta}_d)^T \mathbf{y}$.
- (4) Extract the irregular discriminant features \mathbf{W}_2 . Let $\mathbf{P}_2 = (\alpha_{q+1}, \alpha_{q+2}, \dots, \alpha_m)$, calculate the irregular discriminant feature vector $\mathbf{W}_2 = (\hat{\delta}_1, \hat{\delta}_2, \dots, \hat{\delta}_d)^T \mathbf{y}$.
- (5) Repeat the previous four steps until all integer pixel edge points are taken.

Fuse the regular and the irregular discriminant feature, use similarity measures to classify samples.

4.2. Database of O-rings

In order to select the most appropriate classification algorithm, we established a database of O-rings. The image database that we established consists of five classes including the material shortage class, the bumps class, the dents class, the breakage class and no defects class. Each class consists of fifteen images. We randomly choose ten images as the training samples and the other five images as the testing samples during our experiment. Fig. 10 shows some example of O-rings in our database.

4.3. Comparison of defect classification algorithm

After database creation, we compare three methods in this section for O-rings defect classification, which are KPCA, KFD and CKFD.

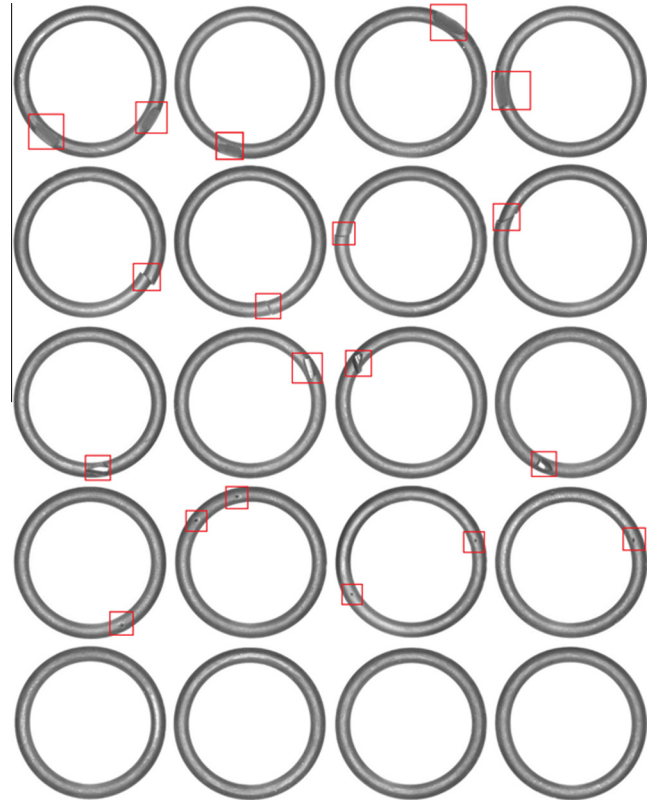


Fig. 10. Example O-ring images in our database.

Fig. 11 shows O-rings classification performance of the KPCA, the KFD, and the CKFD method with polynomial kernel function [19]. The horizontal axis represents the number of features used, and the vertical axis indicates the correct classification rate.

Obviously, the CKFD method outperforms KPCA and KFD method, which shows the CKFD algorithm has high superiority. As classification accuracy rate is not particularly high, we change the kernel function to Gaussian kernel and then run more tests. The result is shown in Fig. 12.

From the Fig. 12, we can see that the performance of CKFD algorithm with Gaussian kernel function didn't shown any significant changes, but it is still higher than that of the other two algorithms. Extract accuracy rate curve of CKFD from Figs. 11 and 12, and plot it in Fig. 13.

As can be seen from Fig. 13, classification accuracy has been significantly improved as the number of features increasing. The result suggests that the CKFD method with Gaussian kernel function can improve O-rings performance. Therefore, we should use the CKFD for the following comparative assessment method with different parameters.

For CKFD, the performance is significantly improved when the discriminant features of Category II are involved [20]. There are two aspects are very important for the accuracy of CKFD classification. One aspect is how to choose similarity measures, this will determine which class the testing samples belong to. Another aspect is the internal parameters of CKFD algorithm, including the fusion coefficient k and the parameter of Gaussian kernel σ^2 . The fusion coefficient indicates proportion of the Category II information in two kinds of discriminant feature information in CKFD.

Fig. 14 shows O-rings classification performance of the method using the three different similarity measures: the L_1 distance measure, the Euclidean distance measure and the cosine similarity measure [21]. The L_1 distance outperforms the other two, followed by the Euclidean distance measure and then the cosine similarity measure. So the L_1 distance measure is chosen as the similarity measure.

The next set of experiments evaluate the effects of fusion coefficient k . Fig. 15 shows classification performance result of CKFD method with different fusion coefficient: $k = 0.6$, $k = 0.7$, $k = 0.8$ and $k = 0.9$. Fig. 15 shows that the fusion coefficient at $k = 0.6$ performs better than the others.

After fixing the similarity measure and the fusion coefficient, we need to determine the parameter of Gaussian kernel σ^2 . Fig. 16 shows that classification performance of the CKFD method

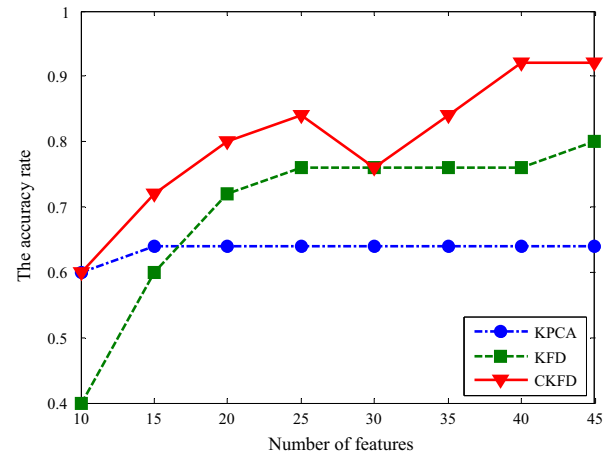


Fig. 12. Classification performance of the KPCA, the KFD, and the CKFD method with Gaussian kernel function.

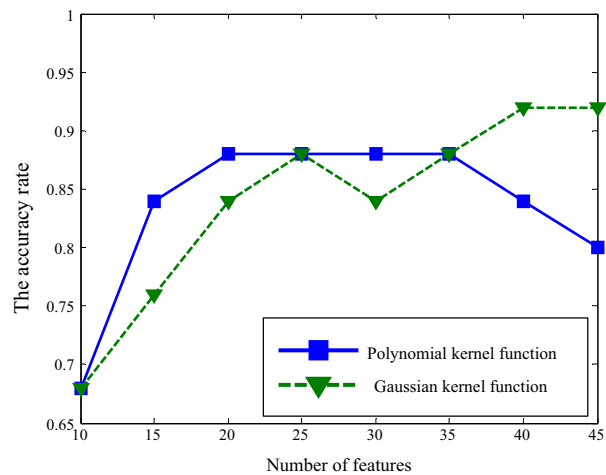


Fig. 13. CKFD method with different kernel functions.

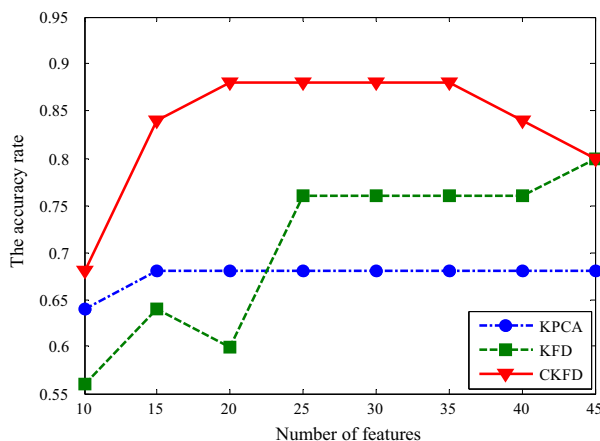


Fig. 11. Classification performance of the KPCA, the KFD, and the CKFD method with polynomial kernel function.

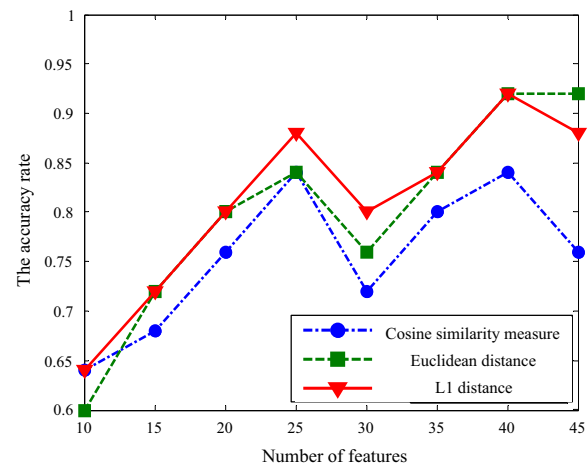


Fig. 14. Classification performance of the CKFD method using three different similarity measures.

with parameter of Gaussian kernel σ^2 : $\sigma^2 = 10^7$, $\sigma^2 = 10^8$, $\sigma^2 = 10^9$. Here we choose the $\sigma^2 = 10^8$ and the number of features as 40, where the highest classification accuracy is obtained.

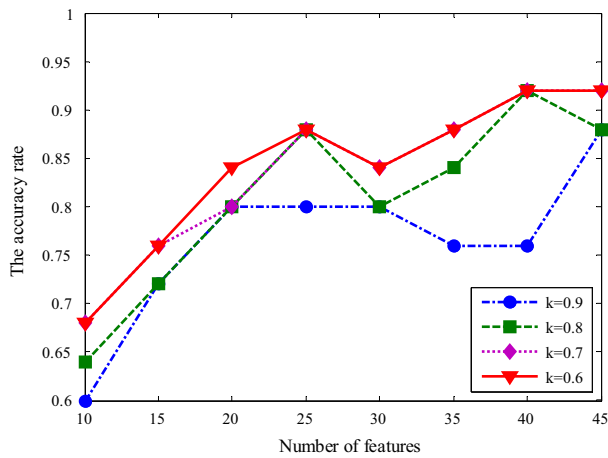


Fig. 15. Classification performance of CKFD method with different fusion coefficient.

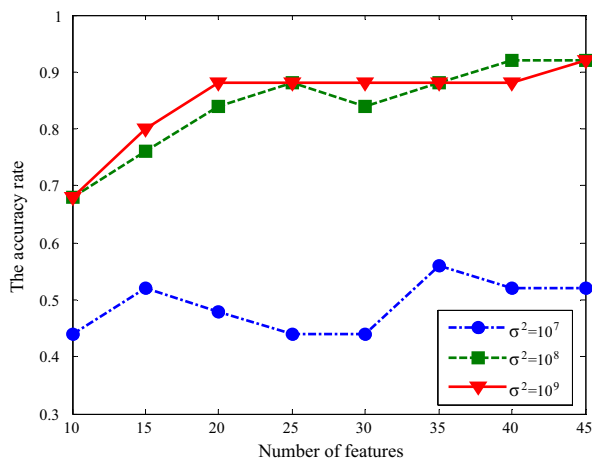


Fig. 16. Classification performance of the CKFD method with different Gaussian parameters.

5. Results and discussion

To evaluate the introduced system, pictures of twenty O-rings with standard inner diameter of 21 mm and thickness of 3 mm were captured for measurement, then the proposed algorithms were applied to each image to calculate the size parameter. A comparison between actual and calculated values of each O-ring parameters are listed in Table 1.

The inner diameter and thickness measurement error are shown in Fig. 17. Among the 20 samples, only one is beyond the tolerance, accounting for 5% and the other 95% are within the range, since the tolerance of 21 mm inner diameter O-rings is ± 0.22 mm. The measurement accuracy was 100%, since the tolerance of 3 mm thickness O-rings is ± 0.1 mm.

We plot the confusion matrix for classification result analyzing in Fig. 18. On the confusion matrix plot, the rows correspond to the predicted class, and the columns show the true class. Class 1–5 respectively corresponding to No defects, Breakage, Bumps, Dents and Material shortage.

In this figure, the diagonal cells show what percentage of the true and predicted classes match. The off diagonal cells show where the classifier has made mistakes. The cell in the bottom right of the plot shows the overall accuracy, while the row at the

Table 1

Comparison between actual and calculated values of each O-ring (mm).

| No. | Actual inner diameter | Actual thickness | Calculated inner diameter | Calculated thickness |
|-----|-----------------------|------------------|---------------------------|----------------------|
| 1 | 21.06 | 3.00 | 21.1264 | 3.0285 |
| 2 | 21.04 | 3.00 | 20.9799 | 3.0221 |
| 3 | 21.08 | 3.00 | 21.1547 | 3.0184 |
| 4 | 21.12 | 3.00 | 20.9598 | 2.9927 |
| 5 | 20.94 | 3.00 | 20.9381 | 3.0172 |
| 6 | 21.12 | 3.00 | 21.1906 | 2.9850 |
| 7 | 20.98 | 3.00 | 21.0216 | 2.9727 |
| 8 | 20.92 | 3.00 | 20.8907 | 3.0136 |
| 9 | 21.10 | 3.00 | 21.1137 | 3.0259 |
| 10 | 21.04 | 3.00 | 21.1658 | 3.0248 |
| 11 | 20.98 | 3.00 | 21.0194 | 3.0594 |
| 12 | 21.04 | 3.00 | 21.1170 | 2.9741 |
| 13 | 21.18 | 3.00 | 21.1271 | 3.0538 |
| 14 | 20.98 | 3.00 | 20.9481 | 3.0562 |
| 15 | 20.92 | 3.00 | 21.0977 | 2.9858 |
| 16 | 21.14 | 3.00 | 21.2854 | 3.0411 |
| 17 | 20.90 | 3.00 | 21.2049 | 3.0204 |
| 18 | 21.06 | 3.00 | 20.9586 | 2.9718 |
| 19 | 21.02 | 3.00 | 21.0180 | 3.0241 |
| 20 | 20.94 | 3.00 | 21.0516 | 3.0427 |

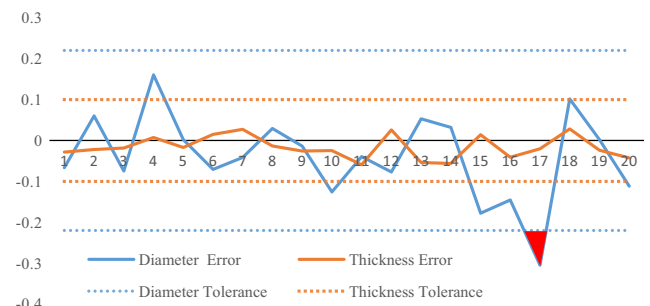


Fig. 17. The measurement error results of diameter and thickness.

| Predict Class | 1 | 15 20.0% | 0 0.0% | 0 0.0% | 1 1.3% | 0 0.0% | 93.8% 6.3% |
|---------------|---|-------------|-------------|-------------|-------------|-------------|----------------|
| | 2 | 0 0.0% | 15 20.0% | 0 0.0% | 0 0.0% | 0 0.0% | 100% 0.0% |
| | 3 | 0 0.0% | 0 0.0% | 14 18.7% | 0 0.0% | 0 0.0% | 100% 0.0% |
| | 4 | 0 0.0% | 0 0.0% | 0 0.0% | 13 17.3% | 1 1.3% | 92.9% 7.1% |
| | 5 | 0 0.0% | 0 0.0% | 1 1.3% | 1 1.3% | 14 18.7% | 87.5% 12.5% |
| | | | | | | | 100% 0.0% |
| | | | | | | | 100% 0.0% |
| | | | | | | | 93.3% 6.7% |
| | | | | | | | 86.7% 13.3% |
| | | | | | | | 93.3% 6.7% |
| | | | | | | | 94.7% 5.3% |
| True Class | | | | | | | |
| 1 | | | | | | | |
| 2 | | | | | | | |
| 3 | | | | | | | |
| 4 | | | | | | | |
| 5 | | | | | | | |

Fig. 18. The classification confusion matrix.

bottom of the plot shows the accuracy for each true class. For example, the rate of O-rings with bumps defect is 93.3% because one of them is detected as material shortage defect incorrectly. Among samples of class with dents defect, two samples are mistakenly classified as no defect and breakage defect, so the rate of this class is 86.7%. Overall, 94.7% of the predictions are correct and 5.3% are wrong classifications.

In addition, we can convert the confusion matrix to 2×2 matrix for each class. Thus, there is recall and precision for each row class. So the F_1 score for each is 0.968, 1, 0.966, 0.897 and 0.903, where an F_1 score reaches its best value at 1 and worst at 0. By analyzing the above result, we can know that accuracy rate for dents defect classification is not very high. This may be due to:

- (1) Features are not obvious with small defect area.
- (2) Lighting condition is quite different at different parts as a result of the uneven surface.
- (3) Features are close to the material shortage defect with big dents area.

6. Conclusion

In order to solve the instable and time consuming problem in detecting O-rings, we proposed an on-line detection system based on computer vision in this paper. For the O-ring measurement, the proposed method obtain a good edge extraction and achieve a suitable precision of fitting circles. Meanwhile, this study presents a machine vision-based inspection method using CKFD to detect four typical defects of the O-rings. The proper recognition rate and classification accuracy was obtained. Finally, practical experiments were carried out to test the correctness of the method. The measurement accuracy rate of inner diameter with 95% and thickness with 100% was achieved. The accurate rate of determination for defect existence can reach 94.67%. The results obtained so far are promising and provide a basis for development of other approaches.

Acknowledgments

This research was supported by National Natural Science Foundation of China (Nos. 51275119 and 50905047) and Self-Planned Task of State Key Laboratory of Robotics and System (HIT) (No. SKLRS201203C). Their supports are gratefully acknowledged.

References

- [1] J. Jurkovic, M. Korosec, J. Kopac, New approach in tool wear measuring technique using CCD vision system, *Int. J. Mach. Tools Manuf.* 45 (9) (2005) 1023–1030.
- [2] E.S. Gadelmawla, Computer vision algorithms for measurement and inspection of spur gears, *Measurement* 44 (9) (2011) 1669–1678.
- [3] H. Shen, S. Li, D. Gu, et al., Bearing defect inspection based on machine vision, *Measurement* 45 (4) (2012) 719–733.
- [4] W. Chang, C. Su, D. Guo, et al., Automated optical inspection for the runout tolerance of circular saw blades, *Int. J. Adv. Manuf. Technol.* 66 (1–4) (2013) 565–582.
- [5] S.S. Martínez, J.G. Ortega, J.G. García, A.S. García, et al., An industrial vision system for surface quality inspection of transparent parts, *Int. J. Adv. Manuf. Technol.* 68 (5–8) (2013) 1123–1136.
- [6] R.A. Bobby, P.S. Sonakar, M. Singaperumal, et al., Identification of defects on highly reflective ring components and analysis using machine vision, *Int. J. Adv. Manuf. Technol.* 52 (1–4) (2011) 217–233.
- [7] L. Li, Z. Wang, F. Pei, Vision-based Surface Defect Inspection for Sequence Circular Objects, *IEEE*, 2012, pp. 1352–1356.
- [8] G.E. Meyer, T. Hindman, K. Laksmi, Machine vision detection parameters for plant species identification, in: G.E. Meyer, J.A. Deshazer (Eds.), *Proceedings of the Society of Photo-optical Instrumentation Engineers (SPIE)*, vol. 3543, 1999, pp. 327–335.
- [9] M.A. Oskoei, H. Hu, A Survey on Edge Detection Methods, University of Essex, UK, 2010.
- [10] J. Canny, A computational approach to edge-detection, *IEEE Trans. Pattern Anal. Mach. Intell.* 8 (6) (1986) 679–698.
- [11] Z. Li, Y. Yang, W. Jiang, Multi-scale morphologic tracking approach for edge detection, *Image Graphics* (2007) 358–362.
- [12] X. Bai, F. Zhou, Edge detection based on mathematical morphology and iterative thresholding, *Lect. Notes Artif. Intell.* 4456 (2007) 953–962.
- [13] A. Fabijanska, A survey of subpixel edge detection methods for images of heat-emitting metal specimens, *Int. J. Appl. Math. Comput. Sci.* 22 (3) (2012) 695–710.
- [14] M. Hagara, P. Kulla, Edge detection with sub-pixel accuracy based on approximation of edge with Erf function, *Radioengineering* 20 (2SI) (2011) 516–524.
- [15] G. Lukcs, R. Martin, D. Marshall, *Faithful Least-squares Fitting of Spheres, Cylinders, Cones and Tori for Reliable Segmentation*, Springer, 1998, pp. 671–686.
- [16] C.J. Liu, Gabor-based kernel PCA with fractional power polynomial models for face recognition, *IEEE Trans. Pattern Anal. Mach. Intell.* 26 (5) (2004) 572–581.
- [17] J. Yang, A.F. Frangi, J.Y. Yang, et al., KPCA plus LDA: a complete kernel Fisher discriminant framework for feature extraction and recognition, *IEEE Trans. Pattern Anal. Mach. Intell.* 27 (2) (2005) 230–244.
- [18] J. Yang, A.F. Frangi, J.Y. Yang, A new kernel Fisher discriminant algorithm with application to face recognition, *Neurocomputing* 56 (2004) 415–421.
- [19] G. Baudat, F.E. Anouar, Generalized discriminant analysis using a kernel approach, *Neural Comput.* 12 (10) (2000) 2385–2404.
- [20] J. Li, J. Pan, Z. Lu, Face recognition using Gabor-based complete Kernel Fisher Discriminant analysis with fractional power polynomial models, *Neural Comput. Appl.* 18 (6) (2009) 613–621.
- [21] V. Athitsos, J. Alon, S. Sclaroff, Efficient Nearest Neighbor Classification Using a Cascade of Approximate Similarity Measures, *IEEE*, 2005.